

**1 Cassini observations of ion and electron beams at**  
**2 Saturn and their relationship to infrared auroral arcs**

S. V. Badman<sup>1,\*</sup>, N. Achilleos<sup>2,3</sup>, C. S. Arridge<sup>3,4</sup>, K. H. Baines<sup>5</sup>,

R. H. Brown<sup>6</sup>, E. J. Bunce<sup>7</sup>, A. J. Coates<sup>3,4</sup>, S. W. H. Cowley<sup>7</sup>,

M. K. Dougherty<sup>8</sup>, M. Fujimoto<sup>1</sup>, G. Hospodarsky<sup>9</sup>, S. Kasahara<sup>1</sup>,

T. Kimura<sup>1</sup>, H. Melin<sup>7</sup>, D. G. Mitchell<sup>10</sup>, T. Stallard<sup>7</sup>, C. Tao<sup>1</sup>

---

<sup>1</sup>JAXA Institute of Space and  
Astronautical Science, Sagami-hara  
252-5210, Japan. Email:  
s.badman@stp.isas.jaxa.jp

<sup>2</sup>Department of Physics and Astronomy,  
University College London, UK

<sup>3</sup>The Centre for Planetary Sciences at  
UCL/Birkbeck, London, UK

<sup>4</sup>Mullard Space Science Laboratory,  
University College London, UK

<sup>5</sup>SSEC, University of Wisconsin-Madison,  
USA

<sup>6</sup>LPL, University of Arizona, USA

<sup>7</sup>University of Leicester, UK

<sup>8</sup>Imperial College London, UK

<sup>9</sup>University of Iowa, USA

<sup>10</sup>APL, Johns Hopkins University, USA

3 **Abstract.** We present Cassini Visual and Infrared Mapping Spectrom-  
4 eter observations of infrared auroral emissions from the noon sector of Sat-  
5 urn's ionosphere revealing multiple intense auroral arcs separated by dark  
6 regions poleward of the main oval. The arcs are interpreted as the ionospheric  
7 signatures of bursts of reconnection occurring at the dayside magnetopause.  
8 The auroral arcs were associated with upward field-aligned currents, the mag-  
9 netic signatures of which were detected by Cassini at high planetary latitudes.  
10 Magnetic field and particle observations in the adjacent downward current  
11 regions showed upward bursts of 100–360 keV light ions in addition to en-  
12 ergetic (100s of keV) electrons, which may have been scattered from upward-  
13 accelerated beams carrying the downward currents. Broadband, upward-propagating  
14 whistler waves were detected simultaneously with the ion beams. The accel-  
15 eration of the light ions from low altitudes is attributed to wave-particle in-  
16 teractions in the downward current regions. Energetic (600 keV) oxygen ions  
17 were also detected, suggesting the presence of ambient oxygen at altitudes  
18 within the acceleration region. These simultaneous in situ and remote ob-  
19 servations reveal the highly energetic magnetospheric dynamics driving some  
20 of Saturn's unusual auroral features. This is the first in situ identification  
21 of transient reconnection events at regions magnetically conjugate to Sat-  
22 urn's magnetopause.

23

## 1. Introduction

24 Early observations of Saturn’s aurorae at ultraviolet (UV) wavelengths suggested they  
 25 formed a narrow ( $1\text{--}2^\circ$ ) ‘main oval’ ring of emission circling the poles at  $\sim 20^\circ$  co-latitude  
 26 [*Broadfoot et al.*, 1981]. Interpretation of auroral images combined with modelling and  
 27 in situ measurements have demonstrated that Saturn’s main oval emissions are generated  
 28 by a field-aligned current system associated with the boundary between open and closed  
 29 magnetic field lines [*Cowley et al.*, 2004; *Badman et al.*, 2006; *Belenkaya et al.*, 2007;  
 30 *Bunce et al.*, 2008a]. In this scenario, the area poleward of the main auroral oval maps to  
 31 open field lines, and its size is determined by the balance between opening of flux at the  
 32 dayside magnetopause and closure in the magnetotail, similar to the terrestrial case.

33 While most of the past studies of Saturn’s aurorae have been made in the UV, especially  
 34 by the Hubble Space Telescope, high spatial resolution images of Saturn’s infrared (IR)  
 35 aurora have been available from the Visual and Infrared Mapping Spectrometer (VIMS,  
 36 *Brown et al.* [2004]) onboard Cassini. For simplicity throughout this study, the term  
 37 ‘IR aurora’ is used to denote  $\text{H}_3^+$  auroral emission, as the wavelength ranges used were  
 38 dominated by  $\text{H}_3^+$  emission lines. To generate IR  $\text{H}_3^+$  emissions, incident auroral electrons  
 39 ionize atmospheric  $\text{H}_2$  to form  $\text{H}_2^+$ , which then reacts with  $\text{H}_2$  to produce the  $\text{H}_3^+$  ionized  
 40 molecule. Ro-vibrational transitions of the  $\text{H}_3^+$  molecule, which has a lifetime of  $\sim 500$  s  
 41 [*Melin et al.*, 2011], produce the IR auroral emissions [*Drossart et al.*, 1989].  $\text{H}_3^+$  emissions  
 42 are strongly dependent on the background temperature and incident electron energy and  
 43 flux [*Tao et al.*, 2011]. Recent analyses of auroral images taken by Cassini have shown

44 Saturn’s main IR auroral emissions to be co-located with those in the UV and thus driven  
45 by the same field-aligned current system [*Badman et al.*, 2011a; *Melin et al.*, 2011].

46 Detailed studies of Saturn’s aurora have revealed a variety of morphologies more compli-  
47 cated than a discrete main oval, which have been related to both the solar wind conditions  
48 and the rotation of the planet [*Clarke et al.*, 2005, 2009; *Crary et al.*, 2005; *Grodent et al.*,  
49 2005, 2011; *Nichols et al.*, 2010]. Some of the most intriguing time-dependent features  
50 are the localised ‘blobs’ and enhanced arcs observed in the noon region, which have been  
51 termed Saturn’s cusp aurora by analogy with observations of the Earth’s aurora. These  
52 features are directly related to the interaction of Saturn’s magnetosphere with the solar  
53 wind [*Gérard et al.*, 2004, 2005; *Bunce et al.*, 2005a]. Transient infrared emissions are  
54 commonly observed poleward of the main oval region and are usually diffuse, but can  
55 cover a range of sizes from small patches to large-scale ‘infilling’ of the polar region [*Stal-*  
56 *lard et al.*, 2004, 2008; *Badman et al.*, 2011a, b]. In this study we report, for the first  
57 time, an IR auroral configuration comprising multiple, distinct arcs poleward of the main  
58 oval in the noon sector.

59 In situ observations of transient reconnection events have not been commonly detected  
60 at Saturn’s magnetopause, unlike spacecraft encounters with the magnetopauses at Earth  
61 [*Rijnbeek et al.*, 1984], Mercury [*Slavin et al.*, 2008] and Jupiter [*Walker and Russell*,  
62 1985]. However, evidence of reconnection in the form of a magnetic field component  
63 normal to Saturn’s magnetopause [*Huddleston et al.*, 1997] and additional heated ion and  
64 electron populations [*McAndrews et al.*, 2008] have been presented. The location and rate  
65 of reconnection depend on the plasma beta parameter on both sides of the magnetopause,  
66 the interplanetary magnetic field (IMF) strength and orientation and the velocity of the

67 solar wind [*Swisdak et al.*, 2003; *Jackman et al.*, 2004; *Bunce et al.*, 2006]. These latter  
68 parameters have also been shown to influence the large-scale behaviour of Saturn's aurora  
69 [*Badman et al.*, 2005; *Cowley et al.*, 2005; *Grodent et al.*, 2005].

70 *Bunce et al.* [2005a] modelled the effects of different IMF conditions on the ionospheric  
71 flows and current systems resulting from pulsed reconnection at both high-latitudes and  
72 the sub-solar magnetopause. As described in their model, at Saturn where the planetary  
73 field is oriented opposite to that of the Earth, reconnection at the sub-solar magnetopause  
74 is expected to occur under conditions of northward IMF, and will produce the following  
75 phenomena: (i) anti-sunward ionospheric flows and currents in the vicinity of the open-  
76 closed boundary (main oval); (ii) the opening of dayside magnetic field lines; and (iii) the  
77 expansion of the dayside auroral oval to lower latitudes. Conversely, high-latitude lobe  
78 reconnection would occur under prolonged southward IMF and result in reversed vortical  
79 flows and currents poleward of the open-closed boundary in the ionosphere. Sub-solar  
80 reconnection is thus related to the intensification of the main auroral arc in the noon  
81 region, while high-latitude reconnection is related to localised auroral emission poleward  
82 of the main oval, whose distributions will be affected by the time-development of the  
83 reconnection [*Bunce et al.*, 2005a; *Gérard et al.*, 2005].

84 Observations of local processes related to Saturn's aurora have also been made in situ  
85 by the Cassini plasma instruments. *Saur et al.* [2006] identified beams of 20–800 keV  
86 electrons accelerated upward from Saturn's ionosphere in the pre-dawn and noon sectors  
87 (the local time (LT) sector explored by Cassini during the studied orbits) and at radial  
88 distances of 11–20  $R_S$ . Similar beams have also been described by *Mitchell et al.* [2009a],  
89 who simultaneously identified energetic upward ions (30–200 keV) and magnetic field

90 perturbations. *Mitchell et al.* [2009a] interpreted these as the signatures of downward  
91 current layers, which were detected at dipole L-shells of 10–50, i.e. incorporating the  
92 statistical auroral and polar cap regions. The events identified by *Mitchell et al.* [2009a]  
93 were observed at a range of local times and could be either steady for hours or pulsed with  
94 a repetition period of tens of minutes. While the discrete aurora are produced by electrons  
95 accelerated downward into the ionosphere (i.e. upward current regions), such downward-  
96 directed current layers (energetic, upward-travelling electrons) have also been identified  
97 in the auroral regions at Earth [*Carlson et al.*, 1998; *Marklund*, 2009] and Jupiter [*Mauk*  
98 *and Saur*, 2007]. Such current layers evidently play an integral role in energy transport  
99 in the auroral regions of these magnetised planets.

100 In this study, in situ measurements of these distinctive downward current signatures  
101 are presented with, for the first time, a simultaneous image of the magnetically-conjugate  
102 auroral region. This enables a direct comparison of the field-aligned currents evident in  
103 the magnetic field and plasma data with the resulting auroral features. In the following  
104 sections, the auroral morphology is described and then related to the relevant in situ  
105 plasma and magnetic field measurements.

## 2. Interval overview: 2008-320 (15 Nov 2008)

106 On day 320 of 2008 (15 Nov 2008) Cassini moved inbound from the dayside magneto-  
107 sphere at high northern latitudes. The trajectory for day of year (DOY) 318–324 in 2008  
108 is shown in Figure 1 in the X–Y and X–Z planes in Kronocentric Solar Magnetospheric  
109 (KSM) coordinates, where X points from Saturn to the Sun, Y is positive towards dusk  
110 and the X–Z plane contains the planetary spin (and magnetic) axis. The ionospheric mag-  
111 netic footprint of Cassini’s trajectory is also shown in the third panel of Figure 1, with

112 the sunward direction towards the right and dawn towards the bottom. The trajectory  
113 has been mapped from Cassini's magnetospheric position using the SOI model of Saturn's  
114 magnetic field [Dougherty *et al.*, 2005] and a model ring current field perturbation [Bunce  
115 *et al.*, 2007]. The ring current perturbation was modelled assuming a nominal magne-  
116 topause standoff distance of 21  $R_S$  and the mapping was performed to 1100 km above the  
117 1-bar reference spheroid. From 1200–2400 UT on day 320, Cassini was at a radial distance  
118 of  $\sim 12 R_S$ , slightly duskward of noon, and moving towards the northern hemisphere at  
119 high latitude. This trajectory thus afforded an excellent view of the northern auroral  
120 region for Cassini imaging instruments.

## 2.1. Infrared auroral images

121 A mosaic of six images of the northern IR aurora taken by VIMS on day 320 is shown in  
122 Figure 2a. VIMS acquires a full wavelength spectrum (0.85–5.1  $\mu\text{m}$ ) at each pixel position  
123 in its field of view (FOV) in turn, where 1 pixel =  $0.5 \times 0.5$  mrad and the FOV for these  
124 observations was  $42 \times 42$  pixels. The total exposure time for each image was  $\sim 30$  min.  
125 The images in Figure 2 have been projected onto a  $0.25^\circ \times 0.25^\circ$  planetocentric polar grid  
126 using an estimated peak emission height of 1100 km above the 1-bar reference spheroid  
127 [Stallard *et al.*, 2011]. The orientation is such that the observer is looking down onto the  
128 pole with the sunward direction (12 LT) at the bottom, dawn (06 LT) to the left and dusk  
129 (18 LT) to the right. The start time of each exposure (UT) is labelled on each image: (i)  
130 1946 UT, (ii) 2018 UT, (iii) 2158 UT, (iv) 2231 UT, (v) 2305 UT and (vi) 2338 UT.

131 The data are colour-coded according to specific intensity, and grey regions are those out-  
132 side the VIMS FOV. Five non-consecutive VIMS wavelength channels containing emission  
133 lines in the range 3.4–3.7  $\mu\text{m}$  have been added to produce these images. The intensities



134 have been corrected for line-of-sight effects using a simple cosine correction (i.e. mul-  
135 tiplication by the cosine of the emission angle for each pixel) and are given in units of  
136  $10^{-5} \text{ W m}^{-2} \mu\text{m}^{-1} \text{ ster}^{-1}$ . The white line shows the ionospheric footprint of Cassini,  
137 mapped from the magnetosphere as described above to 1100 km above the 1-bar refer-  
138 ence spheroid in order to match the auroral projection. White dots mark the ends of the  
139 trajectory at 1200 UT and 2400 UT on 2008-320. The white asterisk marks the footprint  
140 of Cassini at 2200 UT on 2008-320 i.e. the time that image (iii) of this region was taken.

141 Over the  $\sim 4$  h imaging interval, intense and unusual auroral features were observed.  
142 The FOV of the first two images which had start times of (i) 1946 UT and (ii) 2018 UT  
143 partially overlapped, as indicated by the grey outline of the later image in Figure 2a.  
144 Image (i) is therefore reproduced in Figure 2b, with the outline of the following image (ii)  
145 indicated by the dashed white line for reference. Cassini's ionospheric footprint is also  
146 reproduced for clarity in this panel. Considering this first image (i), a wide auroral feature  
147 was observed on the dusk side extending between  $\sim 9^\circ$ – $13^\circ$  co-latitude and across most  
148 of the VIMS FOV:  $\sim 17$ – $21$  LT. The same region captured in image (ii) shows a narrower  
149 ( $\sim 2^\circ$ ) auroral arc, located further from the pole to  $13^\circ$ – $14^\circ$  co-latitude. Comparison of  
150 Figures 2a and b indicates that the intense feature around 18 LT evident in image (i) had  
151 either dimmed or rotated out of the FOV by the time of image (ii). In image (iii) multiple,  
152 discrete arcs were observed in the noon region across  $5^\circ$ – $13^\circ$  co-latitude. The arcs varied  
153 in width and longitudinal extent but were approximately  $1^\circ$  wide and separated by dark  
154 regions. The main oval, taken to be the lowest latitude arc, was very intense (several  
155 times greater than average, *Badman et al.* [2011b]) in the pre-noon region.

156 The next two images which started at (iv) 2231 UT and (v) 2305 UT show sections  
157 of the nightside aurora, where auroral arcs were also visible but at lower intensities than  
158 on the dayside. The two arcs present pre-midnight in image (iv) could plausibly be the  
159 extremity of the same feature observed in image (i), after rotation round to the nightside  
160 at  $\sim 50\%$  of the planetary rotation rate. The last image in the sequence (vi) started at  
161 2338 UT and reveals an intense portion of the main oval post-dawn and at slightly lower  
162 latitude than the adjacent image (iii). The difference in start time between images (iii)  
163 and (vi) was 100 min.

164 The trajectory plotted in Figure 2 shows that Cassini was sampling field lines mapping  
165 to the high-latitude noon sector during this interval. Image (iii) reveals a snapshot of the  
166 conjugate auroral morphology starting at 2158 UT, while the other images which cover  
167 different LT ranges reveal the global dynamics during the interval.

168 Overall this sequence reveals a dynamic aurora, with possible rotating features (e.g. the  
169 post-dusk feature seen in image (i)), equatorward expansion of the oval on the dayside,  
170 and intense arcs poleward of the main oval, all occurring over an interval of less than  
171 5 h UT. The discrete poleward arcs around noon are uncommon in the VIMS data set.  
172 Multiple auroral arcs have been identified in 6 out of 50 sequences of VIMS images studied  
173 so far, where two of these identifications were made in the noon sector. The morphology  
174 of these arcs is similar to bifurcations of the dayside auroral oval seen at the Earth, which  
175 are identified as the ionospheric signatures of newly-opened flux tubes created by dayside  
176 reconnection [*Milan et al.*, 2000]. The apparent equatorward expansion of the dayside  
177 auroral oval seen in this sequence of VIMS images indicates an increase in open flux, thus  
178 supporting this interpretation. The temporal evolution of similar bifurcation features

179 has recently been identified in UV images of Saturn's aurora by *Radioti et al.* [2011]  
180 who related them to transient dayside reconnection events based on their morphology  
181 compared with features seen at Earth. In the following sections the in situ measurements  
182 acquired on 2008-320 are described in relationship to the VIMS auroral observations and  
183 the validity of our proposed transient reconnection interpretation is discussed.

## 2.2. Magnetic field and plasma overview

184 The electron and magnetic field measurements acquired by Cassini at 1200–2400 UT on  
185 2008-320 are plotted in Figure 3. This corresponds to the duration of the trajectory drawn  
186 on the auroral images in Figure 2a. The top panel shows an energy-time spectrogram of  
187 electron differential energy flux measured by the Cassini Plasma Spectrometer - Electron  
188 Spectrometer (CAPS-ELS, *Young et al.* [2004]). The electron energy range covered was  
189 0.5 eV – 28 keV and the fluxes of field-perpendicular (pitch angles 80°–100°) electrons  
190 are plotted. The bottom panel displays the components of the magnetic field in spherical  
191 radial ( $r$ ), polar ( $\theta$ ) and azimuthal ( $\phi$ ) coordinates referenced to the spin (and magnetic)  
192 axis, from which the Cassini model of the internal planetary field [*Dougherty et al.*, 2005]  
193 has been subtracted. The arrows labelled (i) –(vi) at the top of the figure indicate the  
194 start times of the VIMS images shown in Figure 2a.

195 At the start of the interval shown the warm ( $\sim 100$ – $1000$  eV) electron population and  
196 small-scale fluctuations in the magnetic field components were suggestive of Cassini being  
197 on closed field lines. Cassini was at high latitudes at this time ( $\sim 50^\circ$ – $55^\circ$ ) on field  
198 lines mapping to  $\sim 9^\circ$ – $8^\circ$  co-latitude. At around 1730 UT the plasma and field data  
199 abruptly changed; there was a significant decrease in the electron flux at all energies  
200 except at  $< \sim 10$  eV (spacecraft photoelectrons), which may be indicative of the spacecraft

201 crossing from closed to open field lines, and the  $B_\phi$  component in particular showed sharp  
 202 fluctuations. These fluctuations in  $B_\phi$  occurred on  $\sim 1$  h timescales, distinctly shorter  
 203 than the well-known  $\sim 11$  h ‘planetary-period’ oscillations. Perturbations of this nature in  
 204  $B_\phi$  are indicative of field-aligned currents [Talboys *et al.*, 2011], the nature of which will  
 205 now be investigated.

### 2.3. Field-aligned currents

206 The equatorward-directed height-integrated Pedersen current in the ionosphere  $I_P$  can  
 207 be related via Ampère’s law to the  $B_\phi$  component of the magnetic field measured in the  
 208 magnetosphere by

$$I_P = \pm \frac{\rho B_\phi}{\mu_0}, \quad (1)$$

209 where  $\rho$  is the cylindrical radial distance of Cassini from Saturn’s spin axis and the negative  
 210 sign applies for the northern hemisphere (e.g. Bunce *et al.* [2008b]; Talboys *et al.* [2011]).  
 211 This relationship assumes the current ring is azimuthally symmetric, which may not be  
 212 the case for the features studied here but is taken as a reasonable first estimate.  $B_\phi$  and  
 213 the calculated  $I_P$  are shown for the 12 h interval of interest (1200–2400 UT) in the top  
 214 and third panels in Figure 4. The magnetically-mapped ionospheric co-latitude of Cassini  
 215 is plotted in the second panel. The  $\sim 1$  nT fluctuations in  $B_\phi$  are apparent, as are the  
 216 related increases and decreases in  $I_P$ . These fluctuations in  $I_P$  indicate currents flowing  
 217 into or out of the ionosphere. Moving equatorward (right to left in Figure 4) a decrease  
 218 in  $I_P$  requires an upward field-aligned current and an increase in  $I_P$  requires a downward  
 219 field-aligned current. Regions of net decreases and increases in  $I_P$  have been marked by

220 the vertical dashed lines in Figure 4 and labelled a–j, although smaller-scale fluctuations  
 221 are also apparent within these regions.

222 The net upward and downward directed currents  $\Delta I$  in each of the regions a–j have  
 223 been calculated and plotted in the fourth panel of Figure 4. Positive and negative val-  
 224 ues indicate upward and downward field-aligned currents, respectively. The upward and  
 225 downward currents have similar magnitudes of 0.2–0.6 MA rad<sup>-1</sup> but the downward cur-  
 226 rent regions are narrower by a factor of 2–9. This implies that the current densities are  
 227 higher in the downward current regions. The current density just above the ionosphere is  
 228 calculated using

$$j_{\parallel I} = \frac{\Delta I}{R_i^2(\theta_i) \sin \theta_i \Delta \theta_i}, \quad (2)$$

229 where  $R_i$  is the radius of the ionosphere at co-latitude  $\theta_i$ , calculated using an auroral  
 230 surface 1100 km above the 1-bar oblate reference spheroid, and  $\Delta \theta_i$  is the co-latitudinal  
 231 width of the region through which current  $\Delta I$  flows in the ionosphere (e.g. *Bunce et al.*  
 232 [2008b]). The derived values are plotted for regions a–j in the bottom panel of Figure 4.  
 233 The upward current densities are a few hundred nA m<sup>-2</sup> and the downward current  
 234 densities are larger - up to  $\sim 2000$  nA m<sup>-2</sup>. This analysis assumes that the features were  
 235 stationary such that their width was measured by Cassini’s motion across them. In fact,  
 236 as will be discussed further below, the features may be significantly wider than the values  
 237 obtained here and moving faster in the ionosphere than Cassini’s footprint. This means  
 238 that the current density values obtained here may be over-estimated by a factor which  
 239 depends on the real width of the moving features. Opposing this effect is the fact that  
 240 the sharpest changes in  $B_\phi$  occur over shorter timescales (or smaller spatial regions) than

241 the broad current regions a–j defined above. This means that the current density would  
242 be higher than the derived values but in correspondingly smaller regions.

243 This analysis of the magnetic field perturbations indicates that adjacent layers of intense  
244 upward and downward field-aligned currents were encountered by Cassini during this  
245 interval. The asymmetric nature of the signatures (i.e. steep increase, gradual decrease)  
246 suggests that this was a series of structures encountered by Cassini, rather than a single  
247 structure moving back and forth.

#### 2.4. Energetic electron and ion beams

248 After 1200 UT on 2008–320 the Magnetospheric Imaging Instrument (MIMI, *Krimigis*  
249 *et al.* [2004]) Low Energy Magnetospheric Measurements System (LEMMS) and Ion and  
250 Neutral Camera (INCA) instruments detected energetic electrons and ions, respectively.  
251 These data are plotted in the first and fourth panels of Figure 5, respectively, along  
252 with field-parallel ( $0^\circ$ – $20^\circ$  pitch angle, upward) electron fluxes from ELS (second panel),  
253 RPWS electric field spectrogram (third panel) and the field-aligned currents derived above  
254 (bottom panel). In the upper panels the vertical dashed lines mark the boundaries of the  
255 field-aligned current regions plotted in the bottom panel. The labelled arrow at the top  
256 indicates the start time of the VIMS auroral image (iii) shown in Figure 2a.

257 The INCA data in the fourth panel of Figure 5 show the fluxes of light ions, which  
258 may consist of  $H^+$ ,  $H_2^+$ ,  $H_3^+$ ,  $He^+$  ions but these cannot be distinguished from each other  
259 by the instrument. At this time INCA was in neutral mode, meaning it could measure  
260 ions with energies above the collimator plate ion rejection cutoff of  $\sim 180$  keV/q up to the  
261 limit of 360 keV/q. The high-energy light ion fluxes show five distinct peaks of 1–2 orders  
262 of magnitude greater than the interim values. During this interval the spacecraft was

oriented such that INCA could measure field-aligned ions. The pitch-angle distribution of the light ions was strongly focussed within  $\sim 30^\circ$  of the field-parallel (upward from the northern ionosphere) direction.

The ion enhancements were well correlated with the intensifications of the broadband plasma waves shown in the panel above. Most of the wave energy occurred below the electron gyrofrequency (plotted by the white line in Figure 5) indicating that the waves were electromagnetic and propagating in the whistler mode. Poynting vector analysis of the waveforms [*Hospodarsky et al.*, 2001] shows that the waves in these regions were propagating field-aligned i.e. upward from the planet. The narrow beam feature of the ions and the correspondence with the broadband electromagnetic wave enhancements are the same as for the ion conics identified by *Mitchell et al.* [2009a]. At the radial distance sampled in this study,  $\sim 12 R_S$ , the conic structure had collapsed to form a field-aligned beam. There were also some smaller peaks at lower energies e.g. 24–35 keV at  $\sim 2120$ – $2140$  UT. These unusual signatures were actually caused by energetic heavier ions (e.g. oxygen) entering the sensor above the plate cut-off energy and producing a signal corresponding to lower-energy hydrogen ions. The INCA oxygen channels showed a spike at this time for time-of-flight values corresponding to ion energies in the range 250 keV to over 600 keV. The possible origin of these ions will be discussed in the next section.

The LEMMS data (top panel) are shown for an energy range of 200 keV–1 MeV i.e. above the upper limit of the ELS measurements. LEMMS measured several intensifications of electrons between  $\sim 1600$  and 2330 UT, which were strongest at energies up to  $\sim 300$  keV. The intensifications lasted from a few min to  $\sim 40$  min in each case. These were sometimes accompanied by enhancements in the 10 eV–1 keV electrons measured

286 by ELS and visible in the second panel of Figure 5. Bursts of high-energy electrons were  
287 also detected by ELS at  $\sim 2030$  UT and throughout 2100–2340 UT.

288 LEMMS was measuring electrons perpendicular to the magnetic field direction such that  
289 the high-energy electrons it measured cannot be classed as field-aligned beams. However,  
290 previous analyses of similar events have suggested that such electrons have been scattered  
291 from a field-aligned beam into larger pitch-angles [*Mitchell et al.*, 2009a]. ELS covered  
292 pitch angles up to  $\sim 110^\circ$  i.e. the upward field-parallel direction but not the downward  
293 anti-parallel direction. The energetic beams detected by ELS were measured in the upward  
294 direction only; they are not evident in the field-perpendicular fluxes shown in Figure 3.  
295 Past observations have shown both upward and bidirectional electron beams during similar  
296 energetic events [*Saur et al.*, 2006; *Mitchell et al.*, 2009a].

297 The start time of VIMS image (iii), 2158 UT, is marked by the arrow at the top of Fig-  
298 ure 5. At this time Cassini’s ionospheric footprint is indicated by the white asterisk along  
299 the trajectory plotted in Figure 2a. The footprint coincided with an intense poleward au-  
300 roral arc flanked by narrower dark regions at higher and lower latitudes. The field-aligned  
301 current regions plotted in the bottom panel of Figure 5 show that Cassini encountered an  
302 upward field-aligned current at this time, enclosed by narrower downward current regions.  
303 This confirms the auroral arcs were generated at the foot of upward current regions as  
304 expected, while the downward current regions were relatively dark. The relationship of  
305 the plasma observations to the field-aligned current regions will be described next.

### 3. Interpretation of ion and electron beams

306 The field-aligned current regions plotted in the bottom panel of Figure 5 show repeated  
307 adjacent layers of downward and upward currents. The upward ion fluxes and whistler



308 waves exhibit strong enhancements in the downward current regions. The upward acceler-  
309 ation of ionospheric H ions in regions of downward current is consistent with the ‘pressure  
310 cooker’ mechanism, whereby the ions are accelerated perpendicular to the magnetic field  
311 by wave interactions at low altitude until the mirror force overcomes the parallel electric  
312 field trapping them there (e.g. *Carlson et al.* [1998], *Paschmann et al.* [2002]). This pro-  
313 cess leads to a characteristic conic structure of the ions, which collapses to a field-aligned  
314 beam at higher altitudes. These structures have been found in the auroral regions of the  
315 Earth [*Carlson et al.*, 1998; *Marklund*, 2009] and Saturn [*Mitchell et al.*, 2009a].

316 The LEMMS data also showed flux enhancements at up to 100s of keV energies in the  
317 downward current regions, which are interpreted to be the scattered upward-accelerated  
318 electron population. The ELS data showed some enhancements at energies of 10 eV–1 keV  
319 but these were not well correlated with the field-aligned current regions. The ELS data  
320 may not show evidence of the upward electrons carrying the downward current because  
321 the magnitude of the field-aligned voltage was sufficient to accelerate them to energies  
322 above the range detected by ELS ( $<28$  keV). In fact, the high electron energies measured  
323 by LEMMS suggest that the field-aligned voltage was of order  $\sim 10$ – $100$  kV, where wave-  
324 particle interactions and scattering may have also contributed to the energisation of the  
325 electrons.

326 Turning now to the upward current regions, the energetic electron fluxes measured  
327 by LEMMS were reduced in these regions consistent with the downward acceleration of  
328 electrons below the spacecraft. There were some enhancements of the warm electron  
329 population measured by ELS as mentioned above. The ELS field of view did not include  
330 the downward electron population, which was the source of the auroral emission observed.

331 The current carried by the unaccelerated electrons could therefore not be measured in this  
 332 case.

333 Cassini observations made on a different pass through Saturn’s cusp region have sug-  
 334 gested that the current density of the unaccelerated electrons in this region,  $j_{\parallel e}$ , is a few  
 335 tens of  $\text{nA m}^{-2}$  [Bunce *et al.*, 2008a]. This value can be used to estimate the minimum  
 336 altitude of the acceleration region from  $R_{min}/R_i \approx (j_{\parallel I}/j_{\parallel e})^{1/3}$  (assuming a quasi-dipolar  
 337 field, e.g. Cowley *et al.* [2004]). From the magnetic field measurements presented in Fig-  
 338 ure 4,  $j_{\parallel I} \sim 300 \text{ nA m}^{-2}$ . These values yield  $R_{min} \sim 2 R_S$ , well below Cassini’s altitude of  
 339  $\sim 11 R_S$ . This value is in agreement with previous theoretical studies and observations,  
 340 which have placed the acceleration region at  $<1-4 R_S$  above the planet [Cowley *et al.*,  
 341 2004; Mitchell *et al.*, 2009a; Schippers *et al.*, 2011]. Although this estimate is a lower  
 342 limit, it is reasonable to consider that Cassini was above the acceleration region at this  
 343 time so would have only encountered the ambient downward electrons, not the accelerated  
 344 auroral population.

345 ELS also observed some upward beams of  $\sim \text{keV}$  electrons e.g. at  $\sim 2140 \text{ UT}$ ,  $2205 \text{ UT}$ ,  
 346  $2300 \text{ UT}$ . Schippers *et al.* [2011] detected upward electrons in a region of upward field-  
 347 aligned current during an encounter with auroral field lines at Saturn. They related these  
 348 to very fine downward current structures embedded in the broader upward current regions,  
 349 which are also evident as brief fluctuations in  $B_\phi$  within the broad current regions defined  
 350 in the present study (see Figure 4) and may thus explain the energetic electrons observed  
 351 by ELS.

352 Our analysis confirms that ion beams (conics at lower altitudes) were generated in  
 353 regions of downward current identified in the magnetometer data thus supporting the

354 ‘pressure cooker’ acceleration mechanism. The presence of energetic oxygen in the ion  
355 beams suggests that the acceleration region extended sufficiently high along the field  
356 line above the minimum distances quoted above to accelerate the ambient oxygen to the  
357 energies detected.

#### 4. Discussion

358 The intense and distinctive auroral structures observed on 2008-320 suggest that this  
359 was an interval of highly dynamic magnetospheric activity, which is confirmed by the  
360 measurement of energetic ions and electrons on the connected field lines. The location of  
361 the auroral intensifications at and poleward of the open-closed field line boundary (the  
362 poleward edge of the ‘main oval’), suggests that they are associated with the creation  
363 of open flux and its subsequent anti-sunward transport. In this interpretation the noon  
364 section of the main oval intensifies during an interval of magnetopause reconnection [*Bunce*  
365 *et al.*, 2005a; *Gérard et al.*, 2005]. The main auroral arc then bifurcates as the newly-  
366 opened flux is transported anti-sunward (poleward) via the combined effects of solar wind  
367 flow and magnetic tension force on the field line [*Milan et al.*, 2000]. The open-closed  
368 boundary expands equatorward to accommodate the new open flux. If further bursts of  
369 magnetopause reconnection occur, this sequence repeats, leading to a series of auroral arcs  
370 poleward of the main oval, which persist until the newly-created open flux is assimilated  
371 into the tail lobe mapping to the central polar cap. We propose that this is the state that  
372 has been captured by Cassini VIMS in Figure 2a some hours into the bursty reconnection  
373 interval.

374 On the basis of this discussion, the observations are now compared to the model results  
375 for pulsed dayside reconnection at Saturn obtained by *Bunce et al.* [2005a]. First, to

376 estimate the ionospheric velocity of the auroral arcs, Figure 2a shows that the auroral  
377 arcs were  $\sim 1^\circ$  wide and aligned almost perpendicular to Cassini’s anti-sunward and  
378 duskward trajectory. The corresponding upward current regions were encountered by  
379 Cassini for approximately 1 h each (Figure 4). During these encounters Cassini’s footprint  
380 moved approximately  $0.2^\circ$  in the ionosphere. Assuming that the arcs were moving over  
381 Cassini in the same direction as its motion, this yields an ionospheric velocity of  $1.2^\circ$   
382 per hour or  $\sim 300 \text{ m s}^{-1}$ . This corresponds to the ‘fast flow’ model derived by *Bunce*  
383 *et al.* [2005a], applicable to solar wind compression regions during which the dayside  
384 reconnection voltage is  $\sim 400 \text{ kV}$  [*Jackman et al.*, 2004].

385 In the ‘fast flow’ model for sub-solar reconnection, a pair of upward and downward  
386 directed field-aligned currents are predicted during each burst of reconnection with den-  
387 sities of  $300\text{--}1300 \text{ nA m}^{-2}$  and  $70\text{--}1000 \text{ nA m}^{-2}$ , respectively, depending on the sense  
388 of the IMF  $B_Y$  component. These ranges encompass the values measured in the present  
389 study, remembering that the values shown in Figure 4 would be reduced by factors of  
390  $\sim 5\text{--}10$  if the widths of the current layers matched the widths of the intense and dark arcs  
391 seen in Figure 2a, which were approximately  $1^\circ\text{--}0.5^\circ$ . A larger downward current density  
392 than upward current density, as measured here, is obtained in the model for IMF  $B_Y > 0$   
393 conditions.

394 *Bunce et al.* [2005a] also derived the field-aligned voltages and resulting auroral emis-  
395 sions in the upward current regions and found that a potential drop of  $<1\text{--}100 \text{ kV}$  could  
396 be present. In this study the potential drop in the upward current regions cannot be  
397 estimated because of the incomplete electron distribution. The fact that upward light  
398 ions were not detected in the upward current regions suggests that the field-aligned volt-

399 age in these regions was smaller than required to accelerate the ions above the INCA  
400 neutral mode cutoff (180 keV/q). In the downward current regions the electron measure-  
401 ments suggest the presence of upward acceleration through 10s–100s of kV. If the upward  
402 field-aligned voltage was of similar magnitude, the associated UV auroral emissions are  
403 expected to be  $\sim 10$ – $>100$  kR depending on the source electron population [*Bunce et al.*,  
404 2005a]; these are typical to high intensities compared to observations. The lowest latitude  
405 arc shown in image (iii) in Figure 2a was several times more intense than the average IR in-  
406 tensities in this region, while the poleward arcs were of typical ‘polar’ intensities; however  
407 the discrete morphology of the poleward arcs is uncommon [*Badman et al.*, 2011b]. These  
408 observations are consistent with an energetic driving process occurring at the open-closed  
409 field line boundary (lowest latitude arc), which decays over time such that the auroral  
410 currents and emissions on higher-latitude (older) open field lines reduce in intensity as  
411 the field lines are assimilated into the polar cap.

412 Finally, the amount of open flux created during the interval can be estimated by measur-  
413 ing the ionospheric area occupied by the bright arcs poleward of the ‘main oval’. Using the  
414 method for calculating open flux from auroral images described by *Badman et al.* [2005]  
415 and the Cassini model of Saturn’s magnetic field [*Dougherty et al.*, 2005], the amount of  
416 open flux represented by the bright auroral arcs visible within the VIMS FOV shown in  
417 Figure 2a is calculated to be  $\sim 7$  GWb, which is a significant fraction of the total flux typ-  
418 ically threading the polar cap (15–50 GWb, *Badman et al.* [2005]). Dividing this amount  
419 of open flux by the 5 h interval (1700–2200 UT) over which the current signatures were  
420 observed before VIMS image (iii) began gives an average dayside reconnection voltage of

421 390 kV, very similar to the 400 kV quoted above for intervals of strong dayside driving  
422 [*Jackman et al.*, 2004].

423 This value for the reconnection voltage is only an estimate as the duration of the recon-  
424 nection interval and the surface area occupied by the arcs are not known more precisely,  
425 because of Cassini's orbital motion and the incomplete image field-of-view, respectively.  
426 It is in agreement with the apparent equatorward expansion of the auroral oval between  
427 images (iii) and (vi); an expansion of  $\sim 1^\circ$  across the dayside oval as seen between images  
428 (iii) and (vi) would require the addition of  $\sim 2.4$  GWb of open flux. Over the 100 min  
429 interval between images (iii) and (vi), this corresponds to an average reconnection rate  
430 of 400 kV. Note that this estimate compares measurements of the auroral position from  
431 different dayside locations (as VIMS observed different regions in images (iii) and (vi)),  
432 and assumes that a symmetric expansion of the aurora occurred across all dayside LT  
433 over this interval.

434 This voltage estimate is larger than the 250 kV derived by *Radioti et al.* [2011], who  
435 observed a series of poleward auroral arcs over a 2 h interval, indicating stronger driving  
436 by the solar wind in the present study. In fact, 400 kV was the peak reconnection voltage  
437 identified during solar wind compression regions by *Jackman et al.* [2004], suggesting that  
438 the prevailing conditions during this interval were untypical, e.g. that the IMF magnitude  
439 was particularly high. Overall, the similarities of the observations with the *Bunce et al.*  
440 [2005a] model lends weight to the interpretation that the field-aligned currents and auroral  
441 arcs are signatures of multiple bursts of reconnection at the dayside magnetopause under  
442 very strong driving conditions.

443 Saturn’s auroral emissions have also been discussed in relation to vorticity in the mag-  
444 netosphere and at the magnetopause using both global MHD simulations [*Fukazawa et al.*,  
445 2007] and Cassini observations [*Masters et al.*, 2010]. *Fukazawa et al.* [2007] showed large  
446 scale regions of enhanced electron energy flux and field-aligned currents at high latitude  
447 resulting from vortices in the magnetotail or at the magnetopause, but at magnitudes con-  
448 siderably lower than required to produce intense aurora. *Masters et al.* [2010] estimated  
449 the auroral signature of a vortex encountered by Cassini at the low latitude boundary  
450 layer but similarly found that it could only generate emission 10–100 times fainter than  
451 typical main oval intensities. Recent analysis of high-spatial resolution auroral observa-  
452 tions has revealed small spots of UV emission along Saturn’s main auroral region, which  
453 are suggested to be signatures of successive, travelling Kelvin-Helmholtz vortices [*Grodent*  
454 *et al.*, 2011]. Although these UV spots were observed in the near-noon region, like the  
455 IR arcs described in the present study, their morphology was rather different in terms of  
456 both size and latitudinal extent. The IR features described in this study are therefore not  
457 interpreted as signatures of vortices.

458 Pulsed and continuous field-aligned ion beams have been commonly observed by Cassini  
459 at different LT sectors and L-shells [*Mitchell et al.*, 2009a]. While the continuous events  
460 may be associated with relatively steady auroral field-aligned currents, the pulsed events  
461 may be related to pulsed reconnection at different X-line locations as for the event shown  
462 here. On the nightside, intermittent reconnection and energization events have been  
463 observed in Saturn’s magnetotail and are expected to have auroral signatures [*Cowley*  
464 *et al.*, 2005; *Bunce et al.*, 2005b; *Mitchell et al.*, 2009b; *Jackman et al.*, 2010]. During the  
465 interval studied here, several characteristics, including the location of the events, suggest

466 they are related to the solar wind interaction and the conversion between closed and open  
467 flux, but this will not necessarily be the case for all events. Various dynamic processes,  
468 such as flow shears in the low-latitude boundary layer, resulting in auroral field-aligned  
469 currents at different LT and latitudes, could produce similar ion and electron beams, but  
470 the particle energies and auroral intensities would vary according to the local plasma  
471 environment. The global occurrence of these energetic ion and electron beams and their  
472 relationship to auroral features requires further detailed study.

## 5. Conclusions

473 On 2008-320 Cassini VIMS observed IR auroral arcs in the northern noon sector pole-  
474 ward of the main auroral emission. The arcs are interpreted as the ionospheric signatures  
475 of bursts of reconnection occurring at the dayside magnetopause. Each auroral arc was  
476 associated with an upward current i.e. downward flow of electrons into the ionosphere,  
477 the magnetic signatures of which were detected by Cassini during this interval. The  
478 downward electrons carrying the upward currents were not sampled due to incomplete  
479 pitch angle coverage of the plasma instruments but their existence is inferred from the  
480 intense auroral arcs at the ionospheric footprint of the field lines. Magnetic and particle  
481 observations were made in the downward return current regions, in particular upward  
482 bursts of 100–360 keV light ions and energetic (100s of keV) electrons, which may have  
483 been scattered from upward-accelerated beams carrying the downward currents. The  
484 light ions were accelerated from low altitudes via the ‘pressure cooker’ mechanism involv-  
485 ing acceleration perpendicular to the magnetic field below the field-aligned potential by  
486 wave-particle interactions [Mitchell *et al.*, 2009a]. Broadband whistler waves propagating  
487 upward were measured by RPWS coincident with the ion bursts. Energetic (600 keV)



488 oxygen ions were also detected, suggesting the presence of ambient oxygen ions within  
489 the acceleration region. These simultaneous in situ and remote observations reveal the  
490 highly-energetic magnetospheric dynamics driving some of Saturn's uncommon auroral  
491 features. This is the first in situ identification of transient reconnection events at regions  
492 magnetically conjugate to Saturn's magnetopause.

493

494 **Acknowledgments.** This study was facilitated by the Cassini MAG-VIMS collabora-  
495 tion. We acknowledge support of the CAPS ELS science at MSSL-UCL by STFC, and of  
496 the CAPS ELS operations and software team at MSSL-UCL by STFC (to 2010) and by  
497 ESA via UK Space Agency (from 2011). Work at Leicester was supported by STFC grants  
498 ST/H002480/1, ST/G002223/1, and PP/E001130/1. The work at The University of Iowa  
499 was supported by NASA through contract 1415150 with the Jet Propulsion Laboratory.  
500 The authors acknowledge the support of ISSI, as part of this study was discussed by ISSI  
501 International Team 178.

## References

- 502 Arridge, C. S., N. Achilleos, M. K. Dougherty, K. K. Khurana, and C. T. Russell (2006),  
503 Modeling the size and shape of Saturn's magnetopause with variable dynamic pressure,  
504 *J. Geophys. Res.*, *111*(A11), doi:10.1029/2005JA011574.
- 505 Badman, S. V., E. J. Bunce, J. T. Clarke, S. W. H. Cowley, J.-C. Gérard, D. Grodent, and  
506 S. E. Milan (2005), Open flux estimates in Saturn's magnetosphere during the January  
507 2004 Cassini-HST campaign, and implications for reconnection rates, *J. Geophys. Res.*,  
508 *110*(A11), A11216, doi:10.1029/2005JA011240.
- 509 Badman, S. V., S. W. H. Cowley, J.-C. Gérard, and D. Grodent (2006), A statistical  
510 analysis of the location and width of Saturn's southern auroras, *Ann. Geophys.*, *24*(12),  
511 3533–3545.
- 512 Badman, S. V., N. Achilleos, K. H. Baines, R. H. Brown, E. J. Bunce, M. K. Dougherty,  
513 H. Melin, J. D. Nichols, and T. Stallard (2011a), Location of Saturn's northern in-  
514 frared aurora determined from Cassini VIMS images, *Geophys. Res. Lett.*, *38*, doi:  
515 10.1029/2010GL046193.
- 516 Badman, S. V., C. Tao, A. Grocott, S. Kasahara, H. Melin, R. H. Brown, K. H. Baines,  
517 M. Fujimoto, and T. Stallard (2011b), Cassini VIMS observations of latitudinal and  
518 hemispheric variations in Saturn's infrared auroral intensity, *Icarus*, *216*, 367–375, doi:  
519 10.1016/j.icarus.2011.09.031.
- 520 Belenkaya, E. S., I. I. Alexeev, M. S. Blokhina, S. W. H. Cowley, S. V. Badman, V. V.  
521 Kalegaev, and M. S. Grigoryan (2007), IMF dependence of the open-closed field line  
522 boundary in Saturn's ionosphere, and its relation to the UV auroral oval observed by  
523 the Hubble Space Telescope, *Ann. Geophys.*, *25*, 1215–1226, doi:10.5194/angeo-25-1215-

524 2007.

525 Broadfoot, A. L., B. R. Sandel, D. E. Shemansky, J. B. Holberg, G. R. Smith, D. F.  
526 Strobel, J. C. McConnell, S. Kumar, D. M. Hunten, S. K. Atreya, T. M. Donahue, H. W.  
527 Moos, J. L. Bertaux, J. E. Blamont, R. B. Pomphrey, and S. Linick (1981), Extreme  
528 ultraviolet observations from Voyager-1 encounter with Saturn, *Science*, *212*(4491), 206–  
529 211.

530 Brown, R. H., K. H. Baines, G. Bellucci, J. P. Bibring, B. J. Buratti, F. Capaccioni, P. Cer-  
531 roni, R. N. Clark, A. Coradini, D. Cruikshank, P. Drossart, V. Formisano, R. Jaumann,  
532 Y. Langevin, D. L. Matson, T. B. McCord, V. Mennella, E. Miller, R. M. Nelson,  
533 P. D. Nicholson, B. Sicardy, and C. Sotin (2004), The Cassini Visual and Infrared  
534 Mapping Spectrometer (VIMS) investigation, *Space Sci. Rev.*, *115*(1-4), 111–168, doi:  
535 10.1007/s11214-004-1453-x.

536 Bunce, E. J., S. W. H. Cowley, and S. E. Milan (2005a), Interplanetary magnetic field  
537 control of Saturn’s polar cusp aurora, *Ann. Geophys.*, *23*, 1405–1431, doi:10.5194/angeo-  
538 23-1405-2005.

539 Bunce, E. J., S. W. H. Cowley, D. M. Wright, A. J. Coates, M. K. Dougherty, N. Krupp,  
540 W. S. Kurth, and A. M. Rymer (2005b), In situ observations of a solar wind compression-  
541 induced hot plasma injection in Saturn’s tail, *Geophys. Res. Lett.*, *322*, L20S04, doi:  
542 10.1029/2005GL022888.

543 Bunce, E. J., S. W. H. Cowley, C. M. Jackman, J. T. Clarke, F. J. Crary, and M. K.  
544 Dougherty (2006), Cassini observations of the Interplanetary Medium Upstream of Sat-  
545 urn and their relation to the Hubble Space Telescope aurora data, *Adv. Space Res.*, *38*,  
546 806–814, doi:10.1016/j.asr.2005.08.005.

- 547 Bunce, E. J., S. W. H. Cowley, I. I. Alexeev, C. S. Arridge, M. K. Dougherty, J. D. Nichols,  
548 and C. T. Russell (2007), Cassini observations of the variation of Saturn's ring current  
549 parameters with system size, *J. Geophys. Res.*, *112*(A10), doi:10.1029/2007JA012275.
- 550 Bunce, E. J., C. S. Arridge, J. T. Clarke, A. J. Coates, S. W. H. Cowley, M. K. Dougherty,  
551 J.-C. Gérard, D. Grodent, K. C. Hansen, J. D. Nichols, D. J. Southwood, and D. L.  
552 Talboys (2008a), Origin of Saturn's aurora: Simultaneous observations by Cassini and  
553 the Hubble Space Telescope, *J. Geophys. Res.*, *113*(A9), doi:10.1029/2008JA013257.
- 554 Bunce, E. J., C. S. Arridge, S. W. H. Cowley, and M. K. Dougherty (2008b), Magnetic field  
555 structure of Saturn's dayside magnetosphere and its mapping to the ionosphere: Results  
556 from ring current modeling, *J. Geophys. Res.*, *113*(A2), doi:10.1029/2007JA012538.
- 557 Carlson, C. W., J. P. McFadden, R. E. Ergun, M. Temerin, W. Peria, F. S. Mozer,  
558 D. M. Klumpar, E. G. Shelley, W. K. Peterson, E. Moebius, R. Elphic, R. Strangeway,  
559 C. Cattell, and R. Pfaff (1998), FAST observations in the downward auroral current  
560 region: Energetic upgoing electron beams, parallel potential drops, and ion heating,  
561 *Geophys. Res. Lett.*, *25*, 2017–2020, doi:10.1029/98GL00851.
- 562 Clarke, J. T., J.-C. Gérard, D. Grodent, S. Wannawichian, J. Gustin, J. Connerney,  
563 F. Crary, M. Dougherty, W. Kurth, S. W. H. Cowley, E. J. Bunce, T. Hill, and J. Kim  
564 (2005), Morphological differences between Saturn's ultraviolet aurorae and those of  
565 Earth and Jupiter, *Nature*, *433*(7027), 717–719, doi:10.1038/nature03331.
- 566 Clarke, J. T., J. Nichols, J. C. Gerard, D. Grodent, K. C. Hansen, W. Kurth, G. R. Glad-  
567 stone, J. Duval, S. Wannawichian, E. Bunce, S. W. H. Cowley, F. Crary, M. Dougherty,  
568 L. Lamy, D. Mitchell, W. Pryor, K. Retherford, T. Stallard, B. Zieger, P. Zarka, and  
569 B. Cecconi (2009), Response of Jupiter's and Saturn's auroral activity to the solar wind,

- 570 *J. Geophys. Res.*, 114, doi:10.1029/2008JA013694.
- 571 Cowley, S. W. H., E. J. Bunce, and J. M. O'Rourke (2004), A simple quantitative model  
572 of plasma flows and currents in Saturn's polar ionosphere, *J. Geophys. Res.*, 109(A5),  
573 doi:10.1029/2003JA010375.
- 574 Cowley, S. W. H., S. V. Badman, E. J. Bunce, J. T. Clarke, J.-C. Gérard, D. Gro-  
575 dent, C. M. Jackman, S. E. Milan, and T. K. Yeoman (2005), Reconnection in  
576 a rotation-dominated magnetosphere and its relation to Saturn's auroral dynamics,  
577 *J. Geophys. Res.*, 110(A2), doi:10.1029/2004JA010796.
- 578 Crary, F., J. Clarke, M. Dougherty, P. Hanlon, K. Hansen, J. Steinberg, B. Barraclough,  
579 A. Coates, J. Gerard, D. Grodent, W. Kurth, D. Mitchell, A. Rymer, and D. Young  
580 (2005), Solar wind dynamic pressure and electric field as the main factors controlling  
581 Saturn's aurorae, *Nature*, 433(7027), 720–722, doi:DOI 10.1038/nature03333.
- 582 Dougherty, M. K., N. Achilleos, N. André, C. S. Arridge, A. Balogh, C. Bertucci, M. E.  
583 Burton, S. W. H. Cowley, G. Erdos, G. Giampieri, K. H. Glassmeier, K. K. Khurana,  
584 J. Leisner, F. M. Neubauer, C. T. Russell, E. J. Smith, D. J. Southwood, and B. T.  
585 Tsurutani (2005), Cassini magnetometer observations during Saturn orbit insertion,  
586 *Science*, 307(5713), 1266–1270, doi:10.1126/science.1106098.
- 587 Drossart, P., J. P. Maillard, J. Caldwell, S. J. Kim, J. K. G. Watson, W. A. Majewski,  
588 J. Tennyson, S. Miller, S. K. Atreya, J. T. Clarke, J. H. Waite, and R. Wagoner (1989),  
589 Detection of  $H_3^+$  on Jupiter, *Nature*, 340(6234), 539–541.
- 590 Fukazawa, K., S. Ogi, T. Ogino, and R. J. Walker (2007), Magnetospheric convection at  
591 Saturn as a function of IMF BZ, *Geophys. Res. Lett.*, 34(1), doi:10.1029/2006GL028373.

- 592 Gérard, J.-C., D. Grodent, J. Gustin, A. Saglam, J. T. Clarke, and J. T. Trauger (2004),  
593 Characteristics of Saturn's FUV aurora observed with the Space Telescope Imaging  
594 Spectrograph, *J. Geophys. Res.*, *109*(A9), doi:10.1029/2004JA010513.
- 595 Gérard, J.-C., E. J. Bunce, D. Grodent, S. W. H. Cowley, J. T. Clarke, and S. V. Badman  
596 (2005), Signature of Saturn's auroral cusp: Simultaneous Hubble Space Telescope FUV  
597 observations and upstream solar wind monitoring, *J. Geophys. Res.*, *110*(A11), doi:  
598 10.1029/2005JA011094.
- 599 Grodent, D., J.-C. Gérard, S. W. H. Cowley, E. J. Bunce, and J. T. Clarke (2005),  
600 Variable morphology of Saturn's southern ultraviolet aurora, *J. Geophys. Res.*, *110*(A7),  
601 doi:10.1029/2004JA010983.
- 602 Grodent, D., J. Gustin, J.-C. Gérard, A. Radioti, B. Bonfond, and W. R. Pryor  
603 (2011), Small-scale structures in Saturn's ultraviolet aurora, *J. Geophys. Res.*, *116*,  
604 doi:10.1029/2011JA016818.
- 605 Hospodarsky, G. B., T. F. Averkamp, W. S. Kurth, D. A. Gurnett, M. Dougherty,  
606 U. Inan, and T. Wood (2001), Wave normal and Poynting vector calculations using  
607 the Cassini radio and plasma wave instrument, *J. Geophys. Res.*, *106*, 30,253–30,270,  
608 doi:10.1029/2001JA900114.
- 609 Huddleston, D. E., C. T. Russell, G. Le, and A. Szabo (1997), Magnetopause structure  
610 and the role of reconnection at the outer planets, *J. Geophys. Res.*, *1022*, 23,289–+.
- 611 Jackman, C. M., N. Achilleos, E. J. Bunce, S. W. H. Cowley, M. K. Dougherty, G. H.  
612 Jones, S. E. Milan, and E. J. Smith (2004), Interplanetary magnetic field at  $\sim 9$  AU  
613 during the declining phase of the solar cycle and its implications for Saturn's magneto-  
614 spheric dynamics, *J. Geophys. Res.*, *109*(A11), doi:10.1029/2004JA010614.

- 615 Jackman, C. M., C. S. Arridge, J. A. Slavin, S. E. Milan, L. Lamy, M. K. Dougherty, and  
616 A. J. Coates (2010), In situ observations of the effect of a solar wind compression on  
617 Saturn's magnetotail, *J. Geophys. Res.*, *115*, A10,240, doi:10.1029/2010JA015312.
- 618 Krimigis, S. M., D. G. Mitchell, D. C. Hamilton, S. Livi, J. Dandouras, S. Jaskulek, T. P.  
619 Armstrong, J. D. Boldt, A. F. Cheng, G. Gloeckler, J. R. Hayes, K. C. Hsieh, W.-H.  
620 Ip, E. P. Keath, E. Kirsch, N. Krupp, L. J. Lanzerotti, R. Lundgren, B. H. Mauk,  
621 R. W. McEntire, E. C. Roelof, C. E. Schlemm, B. E. Tossman, B. Wilken, and D. J.  
622 Williams (2004), Magnetosphere Imaging Instrument (MIMI) on the Cassini Mission to  
623 Saturn/Titan, *Space Sci. Rev.*, *114*, 233–329, doi:10.1007/s11214-004-1410-8.
- 624 Marklund, G. T. (2009), Electric fields and plasma processes in the auroral downward  
625 current region, below, within, and above the acceleration region, *Space Sci. Rev.*, *142*,  
626 1–21, doi:10.1007/s11214-008-9373-9.
- 627 Masters, A., N. Achilleos, M. G. Kivelson, N. Sergis, M. K. Dougherty, M. F. Thomsen,  
628 C. S. Arridge, S. M. Krimigis, H. J. McAndrews, S. J. Kanani, N. Krupp, and A. J.  
629 Coates (2010), Cassini observations of a Kelvin-Helmholtz vortex in Saturn's outer  
630 magnetosphere, *J. Geophys. Res.*, *115*, A07,225, doi:10.1029/2010JA015351.
- 631 Mauk, B. H., and J. Saur (2007), Equatorial electron beams and auroral structuring at  
632 Jupiter, *J. Geophys. Res.*, *112*, A10,221, doi:10.1029/2007JA012370.
- 633 McAndrews, H. J., C. J. Owen, M. F. Thomsen, B. Lavraud, A. J. Coates, M. K.  
634 Dougherty, and D. T. Young (2008), Evidence for reconnection at Saturn's magne-  
635 topause, *J. Geophys. Res.*, *113*(A4), doi:10.1029/2007JA012581.
- 636 Melin, H., T. Stallard, S. Miller, J. Gustin, G. M., S. V. Badman, W. R. Pryor,  
637 J. O'Donoghue, R. H. Brown, and K. H. Baines (2011), Simultaneous Cassini VIMS

- 638 and UVIS observations of Saturn's southern aurora: comparing emissions from H, H<sub>2</sub>  
639 and H<sub>3</sub><sup>+</sup> at a high spatial resolution, *Geophys. Res. Lett.*, *38*, doi:10.1029/2011GL048457.
- 640 Milan, S. E., M. Lester, S. W. H. Cowley, and M. Brittnacher (2000), Convection and  
641 auroral response to a southward turning of the IMF: Polar UVI, CUTLASS, and IMAGE  
642 signatures of transient magnetic flux transfer at the magnetopause, *J. Geophys. Res.*,  
643 *105*, 15,741–15,756, doi:10.1029/2000JA900022.
- 644 Mitchell, D. G., W. S. Kurth, G. B. Hospodarsky, N. Krupp, J. Saur, B. H. Mauk, J. F.  
645 Carbary, S. M. Krimigis, M. K. Dougherty, and D. C. Hamilton (2009a), Ion conics  
646 and electron beams associated with auroral processes on Saturn, *J. Geophys. Res.*, *114*,  
647 A02,212, doi:10.1029/2008JA013621.
- 648 Mitchell, D. G., S. M. Krimigis, C. Paranicas, P. C. Brandt, J. F. Carbary, E. C.  
649 Roelof, W. S. Kurth, D. A. Gurnett, J. T. Clarke, J. D. Nichols, J.-C. Gérard,  
650 D. C. Grodent, M. K. Dougherty, and W. R. Pryor (2009b), Recurrent energization  
651 of plasma in the midnight-to-dawn quadrant of Saturn's magnetosphere, and its rela-  
652 tionship to auroral UV and radio emissions, *Planet. Space. Sci.*, *57*, 1732–1742, doi:  
653 10.1016/j.pss.2009.04.002.
- 654 Nichols, J. D., B. Cecconi, J. T. Clarke, S. W. H. Cowley, J.-C. Gérard, A. Grocott,  
655 D. Grodent, L. Lamy, and P. Zarka (2010), Variation of Saturn's UV aurora with SKR  
656 phase, *Geophys. Res. Lett.*, *37*, doi:10.1029/2010GL044057.
- 657 Paschmann, G., S. Haaland, and R. Treumann (2002), In situ measurements in the auroral  
658 plasma, in *Auroral plasma physics*, vol. 103, pp. 93–208, Space Science Reviews, doi:  
659 10.1023/A:1023030716698.



- 660 Radioti, A., D. Grodent, J.-C. Gérard, S. E. Milan, B. Bonfond, J. Gustin, and W. R.  
661 Pryor (2011), Bifurcations of the main auroral ring at Saturn: ionospheric signatures  
662 of consecutive reconnection events at the magnetopause, *J. Geophys. Res.*, *116*(A11),  
663 doi:10.1029/2011JA016661.
- 664 Rijnbeek, R. P., S. W. H. Cowley, D. J. Southwood, and C. T. Russell (1984), A survey of  
665 dayside flux transfer events observed by ISEE 1 and 2 magnetometers, *J. Geophys. Res.*,  
666 *89*, 786–800, doi:10.1029/JA089iA02p00786.
- 667 Saur, J., B. H. Mauk, D. G. Mitchell, N. Krupp, K. K. Khurana, S. Livi, S. M. Krimigis,  
668 P. T. Newell, D. J. Williams, P. C. Brandt, A. Lagg, E. Roussos, and M. K. Dougherty  
669 (2006), Anti-planetward auroral electron beams at Saturn, *Nature*, *439*, 699–702, doi:  
670 10.1038/nature04401.
- 671 Schippers, P., C. S. Arridge, J. D. Menietti, D. A. Gurnett, L. Lamy, B. Cecconi,  
672 D. G. Mitchell, N. André, W. S. Kurth, S. Grimald, M. K. Dougherty, A. J. Coates,  
673 N. Krupp, and D. T. Young (2011), Auroral electron distributions within and close  
674 to the Saturn kilometric radiation source region, *J. Geophys. Res.*, *116*, A05,203, doi:  
675 10.1029/2011JA016461.
- 676 Slavin, J. A., M. H. Acuña, B. J. Anderson, D. N. Baker, M. Benna, G. Gloeckler, R. E.  
677 Gold, G. C. Ho, R. M. Killen, H. Korth, S. M. Krimigis, R. L. McNutt, L. R. Nittler,  
678 J. M. Raines, D. Schriver, S. C. Solomon, R. D. Starr, P. Trávníček, and T. H. Zurbuchen  
679 (2008), Mercury’s Magnetosphere After MESSENGER’s First Flyby, *Science*, *321*, 85–,  
680 doi:10.1126/science.1159040.
- 681 Stallard, T., S. Miller, M. Lystrup, N. Achilleos, E. J. Bunce, C. S. Arridge, M. K.  
682 Dougherty, S. W. H. Cowley, S. V. Badman, D. L. Talboys, R. H. Brown, K. H.

- 683 Baines, B. J. Buratti, R. N. Clark, C. Sotin, P. D. Nicholson, and P. Drossart (2008),  
684 Complex structure within Saturn's infrared aurora, *Nature*, *456*(7219), 214–217, doi:  
685 10.1038/nature07440.
- 686 Stallard, T. S., S. Miller, L. M. Trafton, T. R. Geballe, and R. D. Joseph (2004),  
687 Ion winds in Saturn's southern auroral/polar region, *Icarus*, *167*, 204–211, doi:  
688 10.1016/j.icarus.2003.09.006.
- 689 Stallard, T. S., H. Melin, S. Miller, S. V. Badman, R. H. Brown, and K. H. Baines (2011),  
690 Peak emission altitude of Saturn's  $H_3^+$  aurora, *Geophys. Res. Lett.*, *submitted*.
- 691 Swisdak, M., B. N. Rogers, J. F. Drake, and M. A. Shay (2003), Diamagnetic suppression  
692 of component magnetic reconnection at the magnetopause, *J. Geophys. Res.*, *108*, 1218,  
693 doi:10.1029/2002JA009726.
- 694 Talboys, D. L., E. J. Bunce, S. W. H. Cowley, C. S. Arridge, A. J. Coates, and M. K.  
695 Dougherty (2011), Statistical characteristics of field-aligned currents in Saturn's night-  
696 side magnetosphere, *J. Geophys. Res.*, *116*(A04213), doi:10.1029/2010JA016102.
- 697 Tao, C., S. V. Badman, and M. Fujimoto (2011), UV and IR auroral emission model  
698 for the outer planets: Jupiter and Saturn comparison, *Icarus*, *213*, 581–592, doi:  
699 10.1016/j.icarus.2011.04.001.
- 700 Walker, R. J., and C. T. Russell (1985), Flux transfer events at the Jovian magnetopause,  
701 *J. Geophys. Res.*, *90*, 7397–7404, doi:10.1029/JA090iA08p07397.
- 702 Young, D. T., J. J. Berthelier, M. Blanc, J. L. Burch, A. J. Coates, R. Goldstein,  
703 M. Grande, T. W. Hill, R. E. Johnson, V. Kelha, D. J. McComas, E. C. Sittler, K. R.  
704 Svenes, K. Szegö, P. Tanskanen, K. Ahola, D. Anderson, S. Bakshi, R. A. Baragiola,  
705 B. L. Barraclough, R. K. Black, S. Bolton, T. Booker, R. Bowman, P. Casey, F. J. Crary,

706 D. Delapp, G. Dirks, N. Eaker, H. Funsten, J. D. Furman, J. T. Gosling, H. Hannula,  
707 C. Holmlund, H. Huomo, J. M. Illiano, P. Jensen, M. A. Johnson, D. R. Linder, T. Lun-  
708 tama, S. Maurice, K. P. McCabe, K. Mursula, B. T. Narheim, J. E. Nordholt, A. Preece,  
709 J. Rudzki, A. Ruitberg, K. Smith, S. Szalai, M. F. Thomsen, K. Viherkanto, J. Vilp-  
710 pola, T. Vollmer, T. E. Wahl, M. Wüest, T. Ylikorpi, and C. Zinsmeyer (2004), Cassini  
711 Plasma Spectrometer Investigation, *Space Sci. Rev.*, *114*, 1–112, doi:10.1007/s11214-  
712 004-1406-4.

**Figure 1.**

Cassini's trajectory and mapped northern ionospheric footprint during 2008 DOY 318–324 (13–19 Nov 2008) in KSM coordinates, where X points from Saturn to the Sun, Y is positive towards dusk and the X-Z plane contains the rotation (and magnetic) axis. The dot-dashed red lines indicate the extreme positions of the magnetopause for solar wind dynamic pressures of 0.01 nPa and 0.1 nPa, obtained from the *Arridge et al.* [2006] model. The third panel shows the ionospheric footprint of Cassini's trajectory with the sunward direction towards the right and dawn towards the bottom. The red dots mark latitudes at intervals of  $10^\circ$  and the noon-midnight and dawn-dusk meridians.

**Figure 2.**

(a) A mosaic of six Cassini VIMS images of Saturn's infrared aurora taken on 2008-320. The start time of each image is marked at its edge: (i) 1946 UT, (ii) 2018 UT, (iii) 2158 UT, (iv) 2231 UT, (v) 2305 UT and (vi) 2338 UT. The white grid marks latitudes at intervals of  $10^\circ$  and the noon-midnight and dawn-dusk meridians. The white line delimited by dots shows Cassini's ionospheric footprint during 1200–2400 UT on 2008-320. The white asterisk marks Cassini's footprint at 2200 UT on DOY 320. (b) Image (i) taken by Cassini VIMS showing the area overlapped by the following image (ii) whose outline is marked by the white dashed line. Cassini's ionospheric footprint is shown again here for clarity.

**Figure 3.**

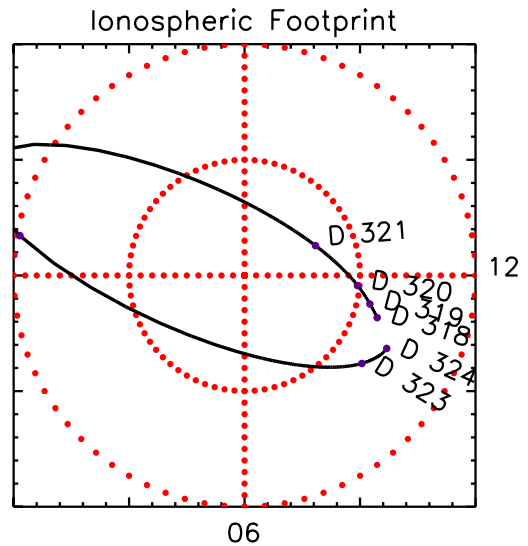
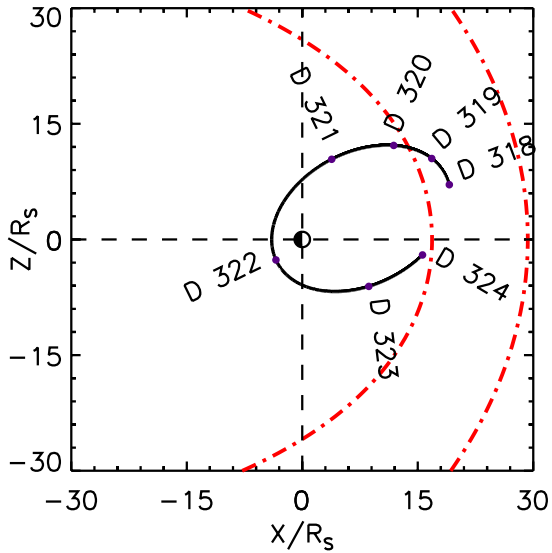
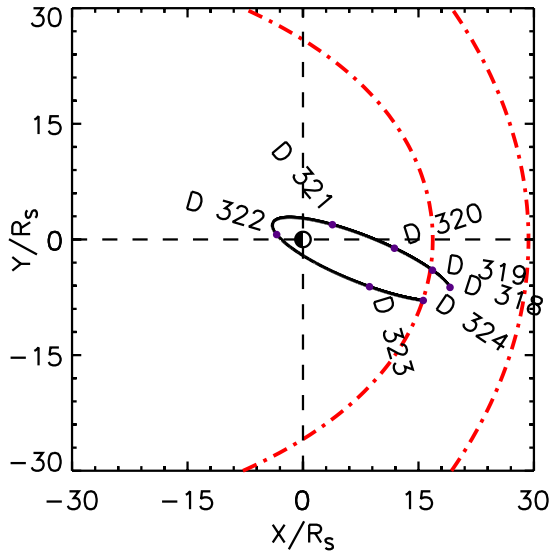
Overview of electron and magnetic field measurements made by Cassini during 1200–2400 UT on 2008–320. The top panel shows the field-perpendicular electron differential energy flux spectrogram from ELS. The bottom panel shows the residual (planetary field model subtracted) components of the magnetic field in spherical radial, polar and azimuthal coordinates. The labelled arrows at the top indicate the start times of the VIMS auroral images (i)–(vi) shown in Figure 2a.

**Figure 4.**

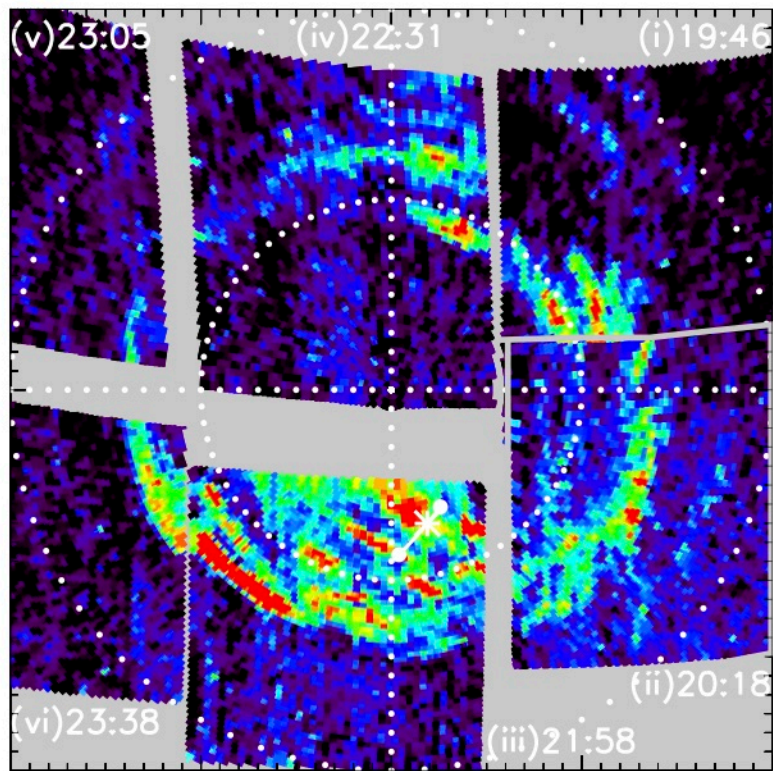
Ionospheric and field-aligned currents. From top to bottom:  $B_\phi$  component of the magnetic field, mapped ionospheric co-latitude of Cassini  $\theta_i$ , height-integrated equatorward ionospheric Pedersen current  $I_P$ , field-aligned current  $\Delta I$ , field-aligned current density just above the ionosphere  $j_{\parallel I}$ . The vertical dashed lines on the third panel delimit regions of net increase and decrease in  $I_P$ , labelled a–j, which are used to calculate  $\Delta I$  and  $j_{\parallel I}$ .

**Figure 5.**

Energetic beams of ions and electrons in regions of field-aligned currents on 2008–320 1200–2400 UT. From top to bottom: fluxes of 200 keV–1 MeV electrons from LEMMS, fluxes of 1 eV – 28 keV field-parallel (upward) electrons from ELS, RPWS electric field spectrogram, ion fluxes measured by INCA, field-aligned current regions determined from MAG data. The vertical dashed lines on the upper panels indicate the boundaries of the upward and downward current regions plotted in the bottom panel. The labelled arrow at the top indicates the start time of VIMS auroral image (iii) shown in Figure 2a.



(a)



12

(b)

